AGU 100 ADVANCING EARTH AND SPACE SCIENCE

AGU Advances

RESEARCH ARTICLE
10.1029/2019AV000140

Cropland Carbon Uptake Delayed and Reduced by 2019 Midwest Floods

Yi Yin[1], Brendan Byrne[2], Junjie Liu[3,1], Paul O. Wennberg[1,4], Kenneth J. Davis[5,6], Troy Magney[1,7], Philipp Köhler[1], Liyin He[1], Rupesh Jeyaram[1], Vincent Humphrey[1], Tobias Gerken[5], Sha Feng[5], Joshua P. Digangi[8], and Christian Frankenberg[1,3]

[1]Division of Geological and Planetary Sciences, California Institute of Technology, Pasadena, CA, USA, [2]NASA Postdoctoral Program Fellow, Jet Propulsion Laboratory, California Institute of Technology, Pasadena, CA, USA, [3]Jet Propulsion Laboratory, California Institute of Technology, Pasadena, CA, USA, [4]Division of Engineering and Applied Science, California Institute of Technology, Pasadena, CA, USA, [5]Department of Meteorology and Atmospheric Science, Pennsylvania State University, University Park, PA, USA, [6]Earth and Environmental Sciences Institute, Pennsylvania State University, University Park, PA, USA, [7]Department of Plant Sciences, Davis, CA, USA, [8]Langley Research Center, National Aeronautics and Space Administration, Hampton, VA, USA

Abstract While large-scale floods directly impact human lives and infrastructures, they also profoundly impact agricultural productivity. New satellite observations of vegetation activity and atmospheric CO_2 offer the opportunity to quantify the effects of such extreme events on cropland carbon sequestration. Widespread flooding during spring and early summer 2019 induced conditions that delayed crop planting across the U.S. Midwest. As a result, satellite observations of solar-induced chlorophyll fluorescence from TROPOspheric Monitoring Instrument and Orbiting Carbon Observatory reveal a 16-day shift in the seasonal cycle of photosynthesis relative to 2018, along with a 15% lower peak value. We estimate a reduction of 0.21 PgC in cropland gross primary productivity in June and July, partially compensated in August and September (+0.14 PgC). The extension of the 2019 growing season into late September is likely to have benefited from increased water availability and late-season temperature. Ultimately, this change is predicted to reduce the crop productivity in the Midwest Corn/Soy belt by ~15% compared to 2018. Using an atmospheric transport model, we show that a decline of ~0.1 PgC in the net carbon uptake during June and July is consistent with observed CO_2 enhancements of up to 10 ppm in the midday boundary layer from Atmospheric Carbon and Transport-America aircraft and over 3 ppm in column-averaged dry-air mole fractions from Orbiting Carbon Observatory. This study quantifies the impact of floods on cropland productivity and demonstrates the potential of combining solar-induced chlorophyll fluorescence with atmospheric CO_2 observations to monitor regional carbon flux anomalies.

Plain Language Summary Widespread flooding and inundation across the U.S. Midwest during spring and early summer 2019 forced many farmers to delay crop planting. New satellite observations of vegetation photosynthesis and atmospheric CO_2 offer the opportunity to quantify the effects of such events on cropland carbon sequestration. We show that the delayed planting resulted in a shift of 16 days in the seasonal cycle of the crop growth and a ~15% lower peak solar-induced chlorophyll fluorescence value. We estimate a reduction of 0.21 PgC in the gross primary production during June and July, partially compensated in August and September (+0.14 PgC). The extension of the 2019 growing season into late September is likely to have benefited from increased water availability and late-season temperature. Ultimately, this change is predicted to reduce the crop production over most of the Midwest Corn/Soy belt by 15%, based on the strong empirical correlation between 2018 growing season SIF and crop yield. The bottom-up estimated net carbon uptake reduction of ~0.1 PgC in June and July is consistently supported by top-down inferred CO_2 anomalies from both aircraft and satellite observations. We anticipate that such a rapid event detection can benefit agricultural and natural resource management and ecological forecasting efforts.

Key Points:
- Flood-induced delay in crop planting shifted the 2019 SIF seasonal cycle by 16 days and reduced the peak value by ~15% compared to 2018
- A ~0.1 PgC reduction in Midwest net ecosystem uptake during June and July is consistent with the observed increase in atmospheric CO_2
- The 2019 flood induced a 0.06 PgC reduction in the annual GPP of croplands (−4%) but a 0.04 PgC increase for natural vegetation (+3%)

Supporting Information:
- Supporting Information S1
- Original Version of Manuscript
- Peer Review History
- First Revision of Manuscript [Accepted]

Correspondence to:
Y. Yin and B. Byrne
yiyin@caltech.edu
brendan.k.byrne@jpl.nasa.gov

Citation:
Yin, Y., Byrne, B., Liu, J., Wennberg, P., Davis, K. J., Magney, T., et al. (2020). Cropland carbon uptake delayed and reduced by 2019 Midwest floods. *AGU Advances*, *1*, e2019AV000140. https://doi.org/10.1029/2019AV000140

Received 6 DEC 2019
Accepted 5 FEB 2020

Peer Review The peer review history for this article is available as a PDF in the Supporting Information.

1. Introduction

Many studies have described the impacts of drought on the carbon cycle (Ciais et al., 2005; Humphrey et al., 2018; J. Liu et al., 2018; Sun et al., 2015; Wolf et al., 2016); however, the impacts of extreme wetness (i.e., floods) have been less well documented. Floods are among the major climate-related disasters that are

projected to increase in a warmer climate (Hirabayashi et al., 2013); quantifying their impact on the terrestrial carbon cycle is critical for the assessment of future climate change impacts. In 2019, the contiguous United States recorded its wettest January to August in 125 years, with wetter-than-normal conditions from the northern Plains to the Gulf Coast (NOAA, October 2019). Vast flooding across the Midwest from March to June forced farmers to significantly delay the planting of crops in this region—known as the Corn Belt—which accounts for ~40% of world corn and soybean production (USDA, 2019). Previous studies have documented the highest peak in photosynthesis across the globe in this area (Guanter et al., 2014; Mueller et al., 2016). Higher net carbon uptake by Midwest cropland compared to the nearby forest has also been shown by tower-based atmospheric CO_2 measurements (Miles et al., 2012), resulting in a large regional carbon sink associated with Midwestern agriculture (Lauvaux et al., 2012; Schuh et al., 2013). Thus, the flood and associated delay in timing of planting is expected to impact the regional carbon cycle; however, it remains unclear to what extent crop growth was affected by the 2019 flood and its consequent impact on the regional carbon cycle.

Satellite observations of solar-induced chlorophyll fluorescence (SIF), a by-product of photosynthesis, have been shown to be a useful proxy of gross primary productivity (GPP) (Frankenberg et al., 2011; Sun et al., 2017; Yang et al., 2015) and crop yield (Guan et al., 2016; Guanter et al., 2014). SIF is mechanistically linked with the light reactions of photosynthesis and has shown close correspondence to GPP across many ecosystems (Frankenberg & Berry, 2018; Gu et al., 2019). As a result of the strong empirical and mechanistic relationship between SIF and GPP at the satellite scale, and confirmation of this at smaller scales (Liu, Guan, et al., 2017), we use SIF as an indicator of GPP (Byrne et al., 2018; Green et al., 2017, 2019; Parazoo et al., 2014). In particular, in the context of floods, the SIF signal is not impaired by surface spectral reflectance properties that are confounded by surface water inundation. The recently launched TROPOspheric Monitoring Instrument (TROPOMI) provides SIF data at unprecedented spatial resolution (7 km × 3.5 km at Nadir) with almost daily global coverage, allowing close monitoring of photosynthesis and carbon uptake as associated events unfold.

From the top-down, measurements of the atmospheric CO_2 can provide constraints on net ecosystem exchange (NEE)—the net exchange of CO_2 between an ecosystem and the atmosphere, determined as autotrophic and heterotrophic respiration minus GPP (Bolin & Keeling, 1963; Gurney et al., 2002; Yin et al., 2018). Space-based measurements of column-averaged dry-air mole fractions of CO_2 (X_{CO2}) have been shown to provide information on NEE anomalies at large subcontinental scales (Byrne et al., 2017; Byrne et al., 2019; Guerlet et al., 2013; Ishizawa et al., 2016; Liu, Bowman, et al., 2017; Liu et al., 2018; Yin et al., 2016) and for point sources (Nassar et al., 2017; Schwandner et al., 2017) but are untested on smaller regional scales, such as the Midwest croplands. The Orbiting Carbon Observatory 2 (OCO-2), launched in 2014, provides X_{CO2} to monitor the atmospheric signal of the event. Boundary layer CO_2 measurements have been shown to provide strong constraints on regional carbon fluxes over the Midwest croplands (Lauvaux et al., 2012; Schuh et al., 2013). The Atmospheric Carbon and Transport (ACT)-America aircraft campaign over the Midwest during summer 2019 provides spatially extensive measurements designed to capture regional atmospheric CO_2 signals.

The combination of these newly available observations offers a unique opportunity to monitor the impacts of 2019 floods on the regional carbon cycle. Specifically, we aim to ask: How does the delayed planting impact the seasonal cycle of the crop growth? What are the implications for the crop productivity of this year? And how does the flooding and inundation impact the overall carbon uptake of these cropping systems? To that end, we first quantify the impact of 2019 floods on the photosynthetic carbon uptake throughout the growing season based on SIF observations relative to the previous years and evaluate potential impacts of this flooding and inundation on crop productivity over the Midwest. Then, we estimate associated atmospheric CO_2 anomaly using a bottom-up approach based on the SIF anomaly and a top-down approach based on satellite and aircraft CO_2 measurements. A schematic for the overview of the methods is shown in Figure S1 in the supporting information.

2. Materials and Methods

2.1. Data

2.1.1. Satellite-Based SIF Observations From TROPOMI and OCO-2

We use satellite-based SIF retrievals to track the progress of photosynthesis. The TROPOMI instrument onboard of the Sentinel 5 Precursor (S-5P) satellite was launched on 13 October 2017. The S-5P satellite flies in

a near-polar Sun-synchronous orbit with an equatorial crossing time at 13:30 local solar time. The TROPOMI instrument has a wide swath of ~2,600 km, yielding almost daily global coverage that allows an unprecedented temporal resolution to track the change in photosynthesis at a given location (Köhler et al., 2018). The spectrometer has a spatial resolution of 7 km along track and 3.5–15 km across track, a spatial resolution that allows us to more appropriately link with county-level agricultural census data. Hence, individual retrievals were aggregated at the county level to align with agricultural census data, as introduced in the section below. A daily correction factor accounting for the diurnal and seasonal variations of solar zenith angle (SZA) is applied to convert an instantaneous SIF signal to a daily average as detailed in Köhler et al., 2018

Additionally, we use SIF retrievals from the Orbiting Carbon Observatory (OCO-2) to complement the TROPOMI SIF records. The OCO-2 instrument has a longer temporal record (since September 2014), providing a multiyear reference of a typical seasonal cycle. Compared to TROPOMI, it has a higher spectral and spatial resolution (1.3 × 2.25 km), and as a trade-off, it has a much sparser sampling coverage in both space (swath width of up to 10 km) and time (with a global revisit time of 16 days; Sun et al., 2017). The two instruments have been shown to be in close agreement for overlapping retrievals (Köhler et al., 2018).

2.1.2. Agricultural Statistics

We obtain county-level crop statistics of 2018 from the United States Department of Agriculture (USDA) National Agricultural Statistics Service (NASS) Quick Stats Database (quickstats.nass.usda.gov), including the planted/harvest area and crop yield of individual crop types. Note that reported crop yield refers to the amount of crop produced per harvested area, whereas crop production refers to the total amount of harvest, which is the sum of crop yield multiplied by harvested area. As satellite observes vegetation productivity per unit area—not necessarily harvested area—we introduce a term "crop productivity" here, specifically referring to the amount of all crops produced per unit area. We add up all reported crops for individual county.

For each county, we calculate the percentage of cropland area and the ratio of C4 to C3 crops. The latter is important to consider because C3 and C4 plants use different photosynthetic pathways, which show a different response of SIF to GPP (Liu, Guan, & Liu, 2017). C4 plants inhibit photorespiration, which results in higher GPP to SIF ratio, as SIF is most sensitive to the light reactions of photosynthesis (Gu et al., 2019). Typical C3 crops include soybeans, wheat, barley, oats, rice, and tree crops, whereas typical C4 crops include corn, sugarcane, and sorghum. Here, we focus on corn and soybeans, which are predominately planted in the Midwest. As the county-level statistics of 2019 are not yet available, we use state-level planted/emerged areas of corn and soybean for 2019 from weekly USDA reports (USDA, 2019); hence, the uncertainty of those reported dates is around 1 week.

2.1.3. Atmospheric CO_2 Observations

To analyze signals of atmospheric CO_2, we use CO_2 observations from both satellites and aircraft. We downloaded Version 9 of the Atmospheric CO_2 Observations from Space OCO-2 lite X_{CO2} retrieval files from the CO_2 Virtual Science Data Environment (https://co2.jpl.nasa.gov/; Crisp et al., 2012). We include land nadir and land glint measurements.

We also use airborne CO_2 measurements from the NASA ACT-America campaign conducted during the summer 2019 over the eastern United States (Digangi et al., 2017). We use observations from a total of 37 campaign flight days over 11 June to 27 July 2019; the campaign schedule is available online (at https://act-america.larc.nasa.gov/). For each campaign, CO_2 was measured from two aircraft in coordinated regional flight patterns using PICARRO G2401-m monitors at 0.4 Hz. The measurements are averaged into a 5-s product, which approximately corresponds to 500-m segments as the plane speed is ~100 m/s. The instrument is calibrated hourly using standards traceable to the WMO X2007 scale (Tans et al., 2017). For analysis, we gridded the raw data to 2° × 2.5° horizontally and 47 layers vertically to match the resolution of the chemical transport model. To reduce the impact of remote sources, we only include data within the atmospheric boundary layer (between 300 and 1,500 m above ground level).

2.1.4. Environmental Variables

We use terrestrial water storage (TWS) anomalies derived from the Gravity Recovery and Climate Experiment (GRACE) and GRACE Follow-On (GRACE-FO) missions (Flechtner et al., 2014; Tapley et al., 2004). TWS anomalies over the U.S. Midwest reflect changes in soil moisture, groundwater, snowpack, and surface waters, mainly in response to climate variability (Humphrey et al., 2016). We use the RL06

monthly mass grids by NASA's Jet Propulsion Laboratory, apply scaling factors (Landerer & Swenson, 2012), and retrieve the regional average TWS anomalies over all regions with crop area fractions larger than 25% over the period April 2002 to August 2019. We note that there is a gap of 12 months between GRACE and GRACE-FO which is still under investigation; however, preliminary analyses indicate that there is no systematic bias between the two missions.

Temperature, vapor pressure deficit and precipitation data are obtained from ERA5 (Copernicus Climate Change Service (C3S), 2019), the fifth-generation atmospheric reanalysis of the European Centre for Medium-Range Weather Forecasts. This reanalysis assimilates multiple data streams from satellite and in situ measurements and provides hourly data at a spatial resolution of 30 km. We compute daily regional averages over all Midwest states with crop area fractions larger than 25% (see mask of the 17 selected states in Figure S4).

2.2. Model

2.2.1. Atmospheric Transport and Flux Inversion Model (GHGF-Flux)

We use an atmospheric transport model to simulate expected signals in the atmospheric CO_2 due to the flood induced anomaly in cropland carbon uptake. We use the forward and adjoint components of the Greenhouse gas framework-Flux model (GHGF-Flux) for atmospheric chemical transport and flux inversion analysis. GHGF-Flux is a flux inversion system developed within NASA's Carbon Monitoring System Flux project (Bowman et al., 2017; J. Liu et al., 2014). GHGF-Flux inherits the chemistry transport model from the GEOS-Chem and the adjoint analysis methods from the GEOS-Chem-adjoint. Chemical transport is driven by the Modern-Era Retrospective Analysis for Research and Applications, Version 2 (MERRA-2) meteorology produced with Version 5.12.4 of the GEOS atmospheric data assimilation system (Gelaro et al., 2017).

In this study, we use GHGF-Flux to perform forward tracer transport at 2° × 2.5° spatial resolution for the year 2019. We also use GHGF-Flux to perform inversions to derive the 2018 baseline NEE at a 4° × 5° spatial resolution. To estimate 2018 NEE, we use the average of three inversions that employ different prior NEE fluxes: SiB3 (Baker et al., 2008), CASA (Potter et al., 1993; James T Randerson et al., 1996; van der Werf et al., 2006), and FLUXCOM (Jung et al., 2017; Tramontana et al., 2016). All versions assimilate OCO-2 land nadir and land glint data from October 2017 to April 2019 to optimize 14-day scaling factors for gridded NEE and ocean fluxes using the approach of Byrne et al. (2019); see Appendix 1 for details. The optimized 2018 NEE was then used to simulate a theoretical baseline for CO_2 mole fractions at 2° × 2.5° driven by 2019 meteorological reanalysis, which represents an ideal case when 2019 carbon fluxes are identical to 2018 while the transport pattern being different. The mismatch between the baseline CO_2 and measured CO_2 provides a measure of the difference in fluxes between years (Figure S6).

2.3. Methods

2.3.1. SIF-Based GPP and NEE Estimates

SIF has been shown to be a robust proxy for GPP (Frankenberg & Berry, 2018; van der Tol et al., 2014). While nonlinear relationships between GPP and SIF have been observed at leaf and flux-tower scales under certain conditions, for example, strong incoming light (Magney et al., 2019; Verma et al., 2017), linear relationships have been generally observed at ecosystem and regional scales (Frankenberg et al., 2011; Li et al., 2018; Magney et al., 2019; Sun et al., 2017). The robust linear relationship at increasing scales is likely because satellite measurements are primarily measuring an integrated canopy average of low Photosynthetically Active Radiation (PAR). At higher light levels, GPP saturates while SIF continues to increase (Magney, Frankenberg, et al., 2019), but it is unlikely that satellite measurements over large pixels are measuring in this light regime. Based on this, and results from previous studies, we quantify GPP using SIF observations (MacBean et al., 2018; Parazoo et al., 2014). Due to the different GPP to SIF slopes between C3 and C4 plants (He et al., in review; Gu et al., 2019; Li et al., 2018; Liu, Guan, & Liu, 2017; Miao et al., 2018; Pérez-Priego et al., 2015), we use different scaling factors for C3 and C4 crops following the linear GPP:SIF ratios for daily averages as documented by Li et al. (2018) (19.8 and 29.4 g $C{\cdot}m^{-2}{\cdot}day^{-1}/Wm^{-2}{\cdot}\mu m^{-1}{\cdot}sr^{-1}$ for C3 and C4, respectively). Thus, for each county the scaling factor is C3/C4 growing area weighted.

For the noncrop area, we use 2018 MODIS MCD12Q1 land cover map (https://doi.org/10.5067/MODIS/MCD12Q1.006) to identify the land cover type at 0.083° spatial resolution into seven different vegetation types, namely, evergreen broadleaf forest, deciduous broadleaf and mixed forest, needleleaf forest, shrub,

woody savanna and savanna, and grasslands. We then apply corresponding GPP:SIF ratios for each vegetation type following (Li et al., 2018), where the ratios are derived from flux tower GPP observations and OCO-2 SIF.

Based on diurnal-cycle-corrected TROPOMI SIF, we estimate daily county-level GPP for every 8-day interval accounting for its planted areas of C3/C4 as documented by USDA. A conversion factor of 0.64 is used to convert TROPOMI SIF at 740 nm to SIF at 757 nm, to account for spectral scaling differences at different wavelengths in the SIF signal retrieval (Köehler et al., 2018). The differences in GPP between 2019 and 2018 (noted as ΔGPP) at the same time of the year are used to estimate the 2019 GPP anomaly.

To estimate the impact on the net carbon exchanges (ΔNEE), we assume that the anomaly is solely induced by a reduction in net primary productivity (NPP), which accounts for about half of GPP following Randerson et al. (1996). Due to the lack of direct observational evidence, we assume no significant changes in heterotrophic respiration between the 2 years. Hence, for further analysis, $\Delta NEE = -0.5 \times \Delta GPP$. To isolate the impact from Midwest cropland on NEE, we only include counties in the 17 states of the Midwest and southern United States whose cropland coverages are larger than 25% for this estimate. We tested that the results are not sensitive to the choice of this threshold as shown in Table S1. Resultant ΔNEE between 2019 and 2018 are aggregated into gridded data at 2° × 2.5° resolution for atmospheric transport model simulation as detailed below.

2.3.2. Flood-Induced Atmospheric CO_2 Signal Estimates

A reduction in NEE is expected to increase atmospheric CO_2 downwind of the croplands. We estimate the anomaly in atmospheric CO_2 by calculating differences in NEE between 2019 and 2018 (denoted as ΔCO_2). The ΔCO_2 signal from this event is calculated using both top-down and bottom-up approaches, and then we evaluate the consistency between the two approaches.

Bottom-up expected ΔCO_2 are simulated from the SIF-inferred ΔNEE using an atmospheric transport model (GHGF-Flux). We use estimated ΔNEE surface fluxes at an 8-day temporal resolution as input and sample modeled CO_2 at the time and location of the ACT-America and OCO-2 measurements. The prior profiles and the averaging kernels of the X_{CO2} measurements are applied.

Top-down inferred ΔCO_2 are calculated as the difference between OCO-2 or ACT-America measurements and the baseline CO_2 simulated with posterior 2018 NEE and 2019 meteorology (as described in section 2.2.1).

3. Delayed Cropland Growing Season Seen by SIF

The monthly distributions of county-level instantaneous SIF values from TROPOMI during the growing season of 2018 and the differences between 2019 and 2018 are shown in Figure 1. For both years, the highest SIF values across the United States occurred in the Midwest in July, demonstrating the highest peak productivity of cropland relative to natural ecosystems. This large-scale signal is consistent with previous space-borne SIF observations from a different instrument (Guanter et al., 2014), while the high-resolution of TROPOMI data provides a new opportunity to look into county-level details at a higher temporal resolution. In the Midwest, the 2019 SIF values are much lower than 2018 in June and July; however, they surpass the 2018 levels in August and September.

The distribution of areas showing significant differences in SIF between the 2 years resembles that of the cropland density as shown on the lower left of Figure 1. The largest differences occurred in the Midwest states that have the longest delay in crop planting as shown on the lower right (Figure 1). For regions with crop area fractions larger than 25%, SIF values in 2019 are 30% and 15% lower than 2018 in June and July, respectively. When looking specifically at areas with higher cropland fractions (>50%), SIF decreased by 47% and 20% for June and July. In contrast, 2019 SIF surpasses the 2018 level slightly in August (+8%) and markedly in September (+50% for counties with crop area >25% and +75% for areas with cropland fraction >50%). The increased growth during late growing season partially compensates for the reduction in the early growing season.

The seasonal cycle of daily TROPOMI SIF during 2018 and 2019 is shown in Figure 2a. By shifting the 2019 SIF time series 16 days ahead, we can see that the growing season lengths of the 2 years are similar but the 2019 seasonal peak values are 15% lower. A large part of the decline could be attributed to changes in solar

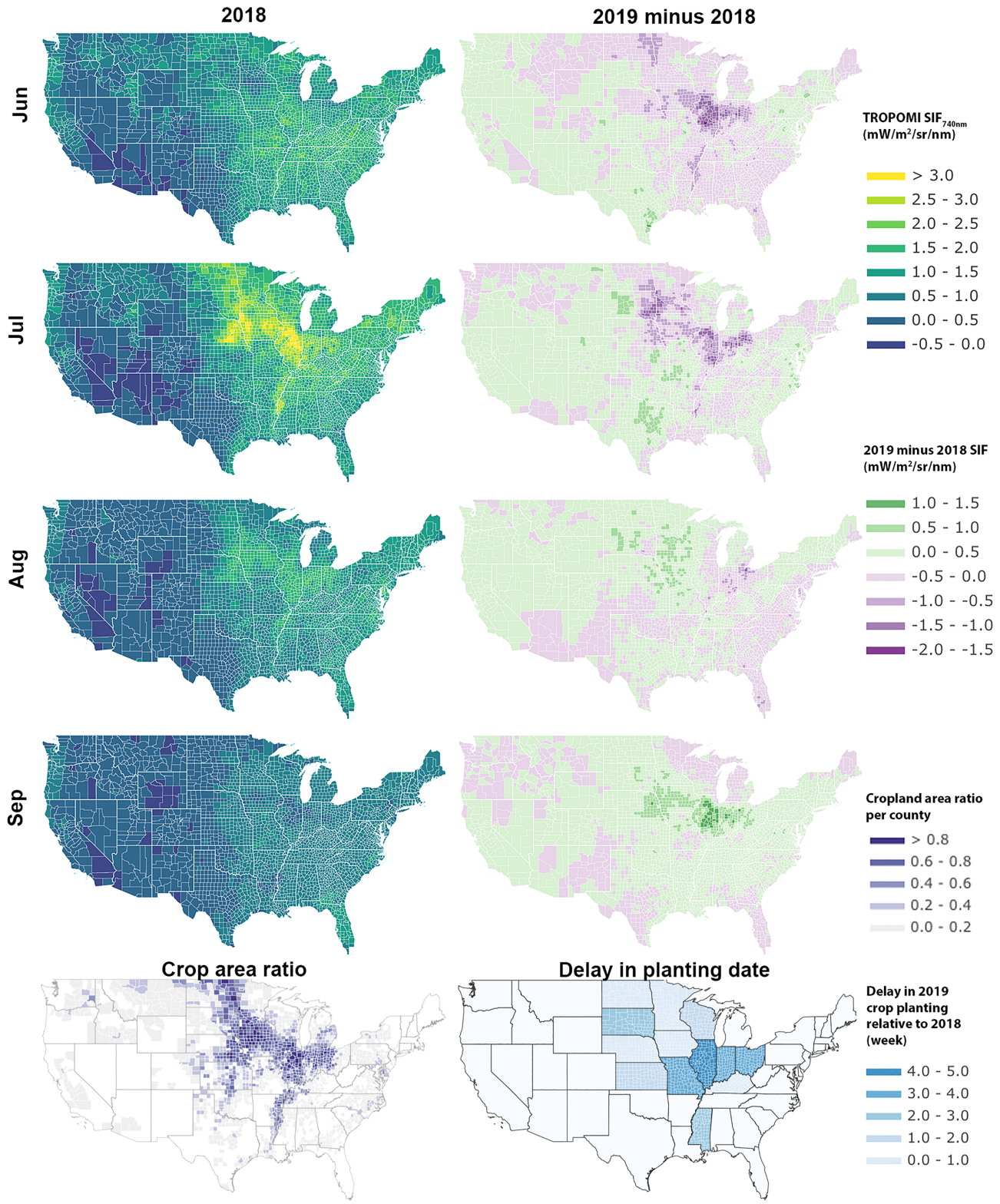

Figure 1. Spatial distribution of instantaneous SIF retrievals from TROPOMI during the main growing seasons in 2018 (the left column) and the differences in SIF between 2019 and 2018 (the right column). The bottom panel shows the cropland area ratio for each county (on the left), and the USDA reported delay in planting 75% of the total planted corn area relative to 2018 (on the right).

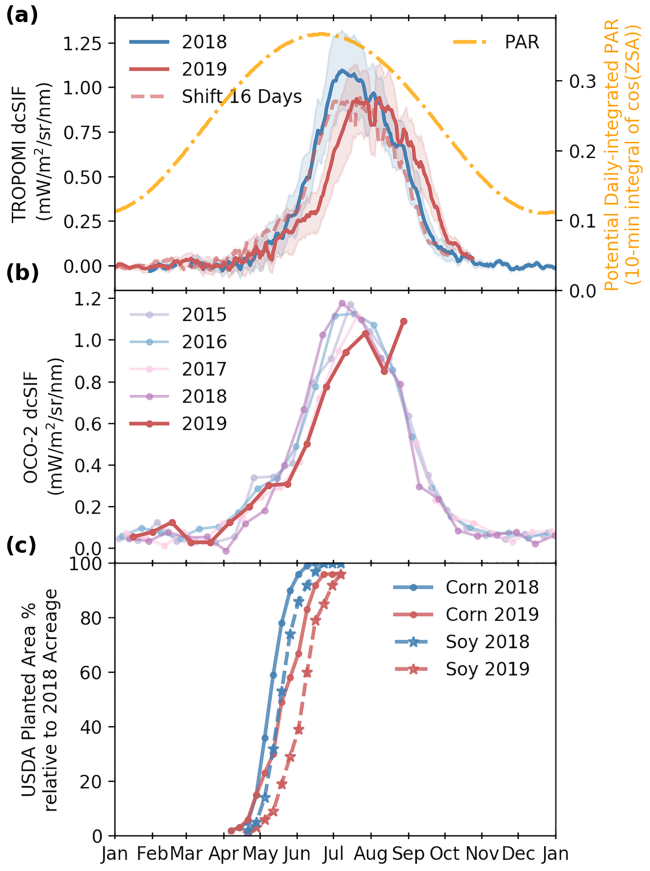

Figure 2. Seasonal cycles of SIF and crop planting date for the Midwest. (a) Four-day running average of 2018 and 2019 daily-corrected TROPOMI SIF over Midwest counties with cropland fraction larger than 50%. The shaded areas represent 1-sigma standard deviations (σ) of the spatial variation across those counties. The seasonal variation in potential PAR due to change in solar zenith angle (SZA) is represented by daily integral of cos (SZA) at 10-min time steps. (b) OCO-2 daily-corrected SIF from 2015 to 2019. Note OCO-2 has sparser spatial and temporal sampling relative to TROPOMI. (c) Percentages of planted area relative to the 2018 total planted area for corn and soy as reported by USDA.

illumination, as the SZA and daytime length decline after the summer solstice. This effect is illustrated by a proxy for seasonal changes in the potential daily PAR under cloud-free conditions using the daily integral of cosine (SZA) at 10-min time steps (Figure 2a). Although the anomalies in TROPOMI SIF shown here are just based on 2 years (2019–2018), analysis of OCO-2 SIF covering the last 5 years (2015–2019) shows that the seasonality of SIF in 2018 is similar to the preceding 3 years but that 2019 is indeed anomalous (Figure 2b). Both data sets reveal a shift in the seasonal cycle and a lower peak SIF value in the growing season of 2019, even though the two instruments have a different temporal and spatial sampling.

Such a delay in the seasonal cycle of crop growth is induced by the late planting of crops as a result of the flood and associated wet soils, which are not conducive to seed germination (anoxic conditions) and are challenging for farm machinery to drive on (Figure 2c). The accumulation of water over the Midwest is reflected in the gradual increase of TWS since the beginning of 2019 as observed by GRACE-FO from space (Figure 3a). The TWS anomaly in June 2019 is around 10 cm higher than that of June 2018, more than two times the standard deviations above the decadal mean as monitored by GRACE. Accumulated precipitation in 2019 is more than one standard deviation above the mean beginning in February and more than two standard deviations above the mean from mid-May onward (Figure S2). By the end of June, the cumulative precipitation is ~13 cm higher than the 40-year average (46 ± 6 cm), a magnitude comparable to the increase in TWS. As a result, the time by which 90% of the corn and soy was planted was delayed by approximately 3 weeks compared to 2018 (Figure 2c). Accordingly, the time by which 90% of the crop had emerged from the soil was delayed by ~3 weeks for corn and ~2 weeks for soybean (Figure S3), consistent with the SIF observations.

The extended 2019 growing season into late September might have been favored by increased water availability as suggested by TWS (+10 cm the decadal mean, Figure 3a) and accumulative precipitation (Figure S2a), as well as a warmer late growing season (+2.5 °C in September, Figure S2b).

4. Estimated Reduction in GPP, Crop Productivity Versus Observed CO_2 Enhancement

Regions with higher cropland ratio show the largest differences in per-area GPP fluxes relative to 2018 (Figure 3b). For the 17 states located in the Midwest and southern United States along the watershed of Missouri and Mississippi rivers (see state mask in Figure S4), GPP reduction is noted from May to July for counties with cropland coverage larger than 10%, with the peak deficit in late June. In contrast, there is a recovery in GPP since early August, with a peak compensation occurring in mid-September. Much smaller differences in SIF-based per-area GPP estimates are observed for the natural vegetation (here defined as regions with cropland coverage <10%), suggesting that unmanaged ecosystems are less sensitive to waterlogged soils that have prevented the planting of crops. Given the large area of noncrop lands over the 17 states, the total GPP anomaly from April to September amounts to a net gain of 0.04 PgC (+3%). As for the croplands (counties in the 17 states with cropland area >10%), we estimate the 2019 anomaly to have led to a reduction of 0.21 PgC in June and July GPP, partially compensated in August and September (+0.14 PgC). Those changes are primarily contributed by areas with cropland coverage >50% (Table S1). The net effect results in a 0.06 PgC reduction in the growing season GPP of croplands (−4%).

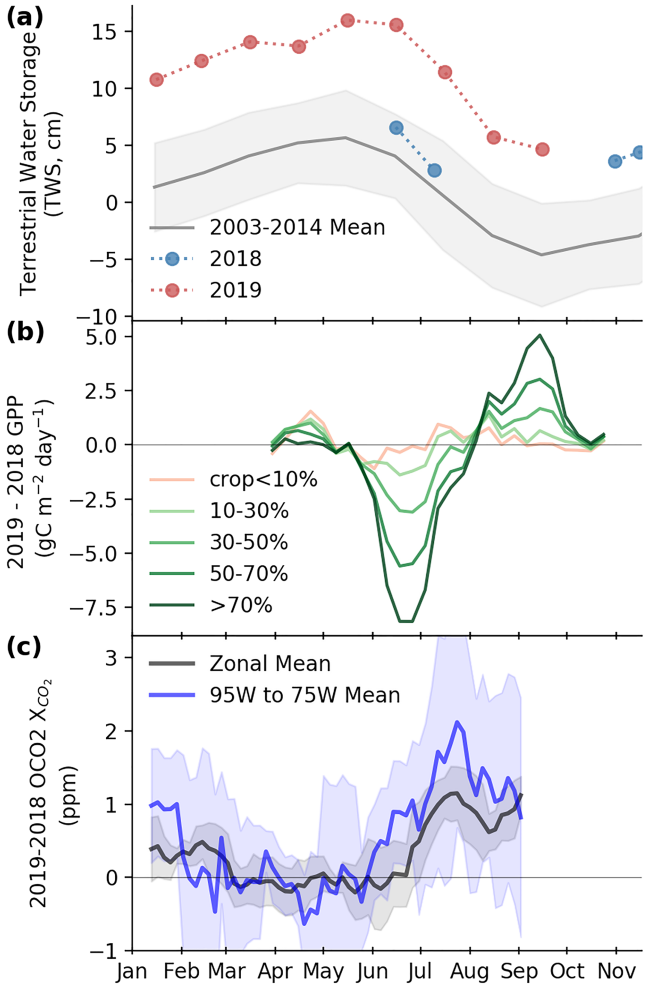

Figure 3. (a) Terrestrial water storage from GRACE-FO (dots, June 2018 to august 2019) and GRACE climatology (2003–2014). The shaded gray area shows the 1-σ of the decadal variations. Note a data gap from August to October 2018. (b) Estimated differences in per area GPP between 2019 and 2018 for regions with different cropland area portions. (c) Differences in detrended OCO-2 X_{CO2} for the zonal mean between 35°–50°N and the subdomain containing the Corn Belt and downwind areas (defined as 75°–95°W). The solid lines show the 24-day running mean of each 4-day average, and the shaded areas show the 1-σ of the 4-day variations within the 24-day window.

In a separate study, we show strong correlations between county-level TROPOMI SIF during the growing season (x, mW·m^{-2}·nm sr^{-1}) and USDA reported crop productivity (y, g/m^2) in 2018, where $y = 968x - 131$ ($R^2 = 0.72$; He et al., in review). The correlation could be further improved when accounting for planted area and C3/C4 contributions ($R^2 = 0.86$). Based on this empirical SIF-crop productivity relationship, we estimate that the 2019 flood results in ~15% decline of crop yield in the Midwest counties with cropland fraction larger than 50% (Figure S5); part of this decline is the result of a decrease in planted crop area (Table S2). Smaller reductions are noted for counties with less dense crop distribution; however, as the relative contribution of crops to the observed SIF signal over a pixel declines, the uncertainty of such estimates increases. We note that this estimate remains speculative as many other factors that are not accounted for in the growing season SIF could contribute to the crop yield at the end of the season. For instance, delayed harvesting can expose crops to unfavorable weather conditions and reduce crop yield (Thomison et al., 2011). In addition, the ratios between the weight of a harvest product and the above ground biomass of the entire plant (commonly noted as harvest index) also change depending on the seed and the environment conditions (Hay, 1995). The allocation of carbon between the below-ground and above-ground biomass may also change given the condition of water and nutrient availability (Hay, 1995). Combining SIF observations with crop models may improve the estimates and forecasting of future crop yield productivity (Guan et al., 2015; Guanter et al., 2014; Somkuti et al., 2020; Zhang et al., 2014).

Unlike the spatially explicit SIF anomalies, the atmosphere is constantly being mixed with a zonal mixing on the timescale of around 2 weeks (Keppel-Aleks et al., 2011, 2012). Hence, we look at differences in the detrended OCO-2 X_{CO2} between 2019 and 2018 (noted as Dif_X_{CO2}) for both the zonal mean over the 35-50°N latitudinal band and for the eastern US domain including the croplands and their downwind area (75-95°W) (Figure 3c). Coincident with the time when negative SIF anomalies emerge, an abrupt increase of ~1 ppm is first observed in the Dif_X_{CO2} over the eastern US domain in late May. Dif_X_{CO2} continues to increase through June and July for both the eastern US and zonal mean domains, with larger anomaly over the eastern US domain than the zonal mean. The regional X_{CO2} enhancement (i.e. the difference between the U.S. domain and the zonal mean) reaches 0.86±0.83 ppm during June. Dif_X_{CO2} start to decline in August when ΔGPP becomes positive. The alignment in the timing of anomalies of X_{CO2} and SIF suggests that reduced uptake over cropland regions is reflected in increased X_{CO2} downwind. However, with such a simple comparison, changes in NEE from other regions between 2019 and 2018 could also contribute to the observed difference in atmospheric CO_2. In addition, differences in atmospheric transport between the two years, as well as in sampling time and location of the observations, could also impact these observed differences in regionally averaged X_{CO2}.

5. Consistent Estimates of Crop Anomalies Between SIF and Atmospheric CO_2

The spatial distribution of the top-down and bottom-up estimates of ΔCO_2 for ACT-America and OCO-2 measurements between 9 June to 18 July 2019 are shown in Figure 4. Bottom-up ΔCO_2 estimates are mostly positive because ΔNEE used for the bottom-up simulation only accounts for Midwest counties with cropland fractions greater than 25%, resulting in reduced net carbon uptake across the region. In contrast, top-down estimated ΔCO_2 are impacted by differences in surface fluxes globally. Nevertheless, positive ΔCO_2 values

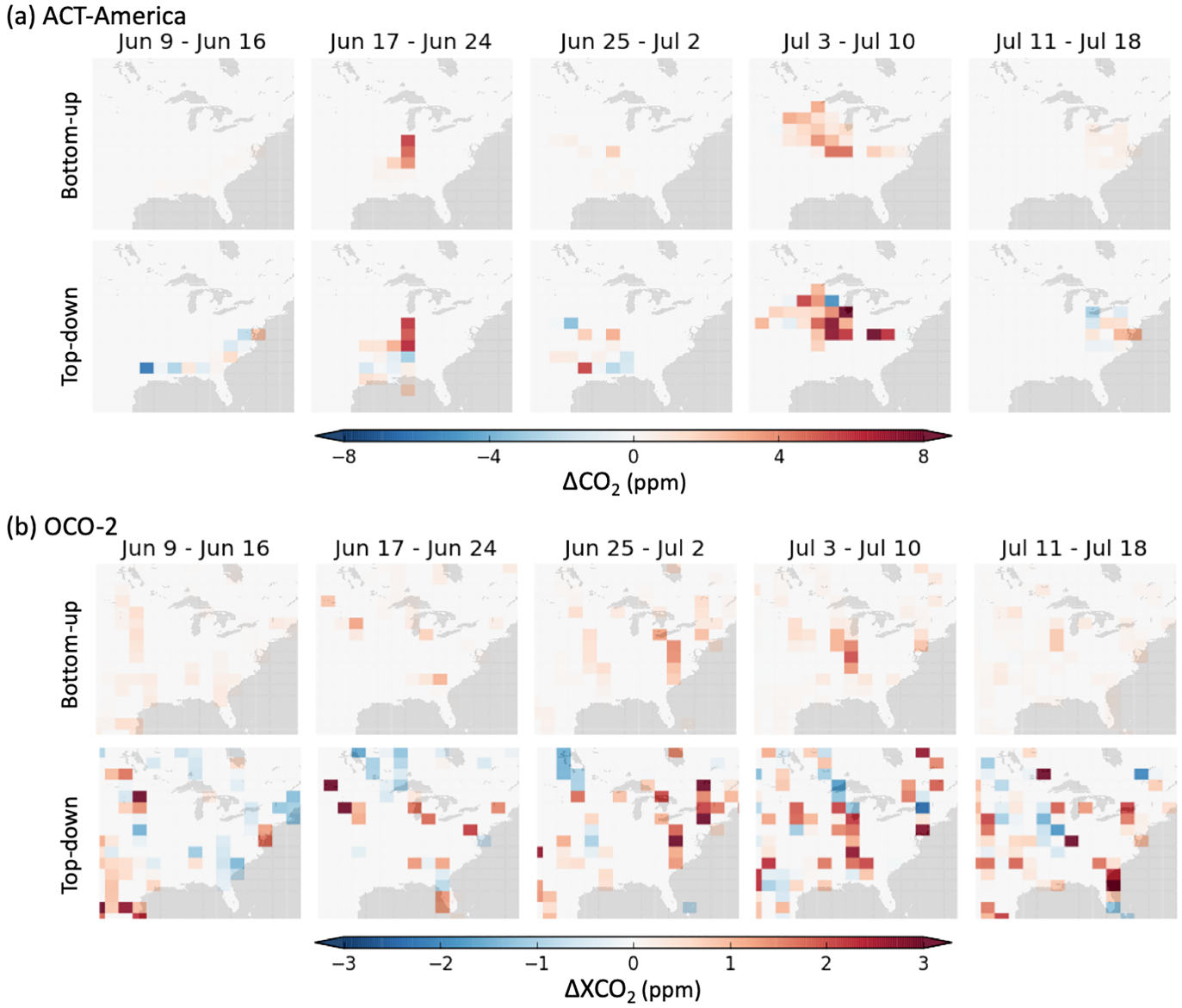

Figure 4. Spatial distribution of top-down and bottom-up ΔCO_2. (a) ACT-America and (b) OCO-2 over 8-day periods from 9 June 2019 to 18 July 2019.

are found over many measurement tracks where the bottom-up method suggests strong CO_2 enhancement. Significant enhancements of CO_2 directly over the Midwest were captured in the flights during Jun 17-24 and July 3-10, with boundary layer ΔCO_2 larger than 10 ppm. The signals are more diluted in other times. Up to 3 ppm of ΔX_{CO2} are observed sometimes over and downwind of the crop region, as OCO-2 measures the column-averaged dry-air mole fraction that are sensitive to a larger source region compared to boundary layer measurements. We note that, for most of June, no X_{CO2} observations directly over the croplands are available due to thick clouds.

Comparing bottom-up and top-down ΔCO_2 estimates at individual model grid and time (Figure 5), we find that bottom-up and top-down ΔCO_2 are in close agreement for both OCO-2 X_{CO2} and ACT-America CO_2 measurements ($P < 0.001$). A linear regression of these data, after aggregating individual observations along the gradient of the predicted ΔCO_2, gives identical slopes of 1.21 for both OCO-2 and ACT-America. A bootstrapping analysis suggests an uncertainty of 0.37 for the slope of OCO-2 regression and 0.07 for the ACT-America regression. The larger uncertainty for OCO-2 comparison may result from the fact that CO_2 signal in the total column is smaller than that in the boundary layer, and hence a lower signal-to-noise

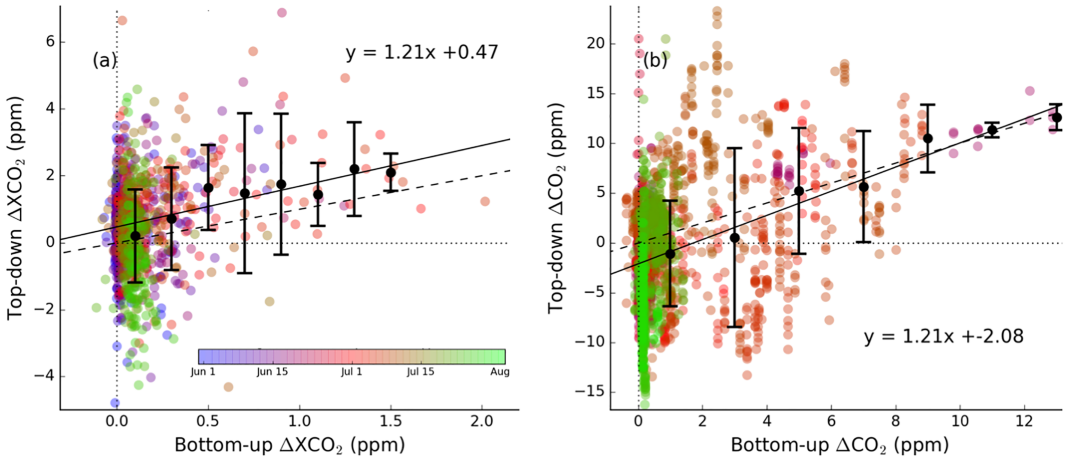

Figure 5. Bottom-up simulated ΔCO2 from SIF-based ΔNEE (*x* axis) versus top-down inferred ΔCO_2 (*y* axis) during June and July 2019. (a) OCO-2 satellite X_{CO2} and (b) ACT-America aircraft measurements within the boundary layer (300–1,500 m). Each point represents CO_2 measurements aggregated within a 2° × 2.5° model grid hourly over the domain of 100–60°W and 20–65°N. the color code represents measurement time. Black points show the average CO_2 anomaly along the bottom-up ΔCO_2 (binned with 0.2 ppm interval for OCO-2 and 2 ppm for ACT-America); the error bars represent 1-sigma standard deviation. The solid line shows the linear regression of the binned data, while the dashed line shows the 1:1 line.

ratio. Besides, the OCO-2 measurements are generally further from the source region (Figure 4) so that the signal has been dispersed by atmospheric transport, while the ACT-America boundary layer measurements are less impacted by remote sources through long range transport (Feng et al., 2019; Keppel-Aleks et al., 2011; Miller et al., 2007). Comparing the aircraft profiles over and outside of the croplands, we can observe a marked enhancement of CO_2 in the boundary layer over the cropland area, which can extend up to ~3,000 m above ground level (Figure S6).

The close agreement between bottom-up and top-down ΔCO_2 demonstrates that our assumption of ΔNEE during the late spring and early summer being primarily driven by GPP reduction is valid. A slope close to one suggests that the magnitude of top-down and bottom-up ΔCO_2 estimates generally agree, which is encouraging considering the simplicity of the method we use. The top-down estimates suggest a ~20% larger anomaly in ΔNEE over this period, we note the following sources for uncertainties.

First, varying GPP:SIF ratios for a certain vegetation type has been reported by different studies (Li et al., 2018; Sun et al., 2018). Future studies that bridge the scales between canopy (flux-tower) and ecosystem (satellite) will be constructive. In addition, we use 2018 planted crop areas for analysis, as the data for 2019 are not yet available, which assumes a static distribution of the C3/C4 component (mostly impacted by soy to corn ratio). Initial USDA state-level survey data for the 12 Midwest states suggest ~13% decrease in planted soybean acreage and only ~1% decrease in planted corn acreage (Table S2), due to the impact of market, flood, and government agricultural assistance policies. There is a roughly 10% increase in the ratio of planted acreage between corn and soy. As the GPP:SIF ratios are higher for C4 plants, we may slight over-estimate the ΔGPP due to a higher C4/C3 ratio in 2019.

Second, the approximation of ΔNEE as $-0.5 \times \Delta GPP$ is highly simplistic. Although photosynthetic uptake dominates the net carbon exchanges in croplands during the growing season, the carbon use efficiency (NPP/GPP) may change depending on the environment conditions (Byrne et al., 2018; Keenan et al., 2019; Wehr et al., 2016). In the context of flooding and soil inundation, CO_2 emissions from soil respiration are likely to be impacted due to anaerobic conditions of the soil; however, it is unclear how to estimate such impact robustly. Future studies using terrestrial carbon cycle models may better estimate the impact of climate variability on heterotrophic respiration.

Third, we use a global transport model to estimate the expected signal in atmospheric CO_2 at a 2×2.5 spatial resolution, which may not be representative of local enhancement as seen by the atmospheric observations. The good agreement between bottom-up and top-down estimates for both ACT-America and OCO-2

suggests that the ΔCO_2 estimates are not very sensitive to systematic transport model errors, as transport errors often impact the boundary layer and total column differently (Basu et al., 2018; Schuh et al., 2019). The coarse spatial resolution of the model we use has limitations in representing fine-scale structures in atmospheric CO_2 (representativeness errors) and aggregating the high-resolution spatial distributions of ΔNEE to the transport model resolution also smooths out the intensity of anomalies (aggregation errors). Using a higher-resolution model could better simulate small-scale structures that atmospheric CO_2 measurements are sensitive to. In addition, changes in other source regions, such as an overall cooler spring in 2019 over North America, may result in changes in top-down ΔCO_2, which was unrelated to the cropland ΔNEE anomaly.

Lastly, observational coverage remains a challenging factor: Much of the area experiencing floods was cloudy in June preventing direct X_{CO2} measurements over the source region, while aircraft campaigns only cover a short period. Previous modeling studies have shown that SIF measurements are less impacted by clouds than X_{CO2} measurements (Frankenberg et al., 2012); the nearly daily global coverage of TROPOMI SIF also allows more cloud-free scenes compared to the revisit time of 16 days. Here, we find that the bottom-up SIF-based ΔCO_2 signals are remarkably consistent with top-down estimates at locations that are sensitive to the sources of the SIF anomaly. As a proof of concept, this study suggests such methods could be applied to other regions where the bottom-up simulated XCO_2 signals on the order of 1 ppm. Future space-based SIF and X_{CO2} missions that have increased measurement frequency and coverage would improve this capability, for instance, geostationary missions like GEOCarb (Moore et al., 2018).

6. Conclusions and Perspectives

We show that the extreme wetness due to flooding and inundation in the Midwest United States during spring and early summer 2019 has caused major disruptions to the agricultural ecosystem, which can be monitored from both vegetation activity as reflected by SIF and from atmospheric CO_2 that reflects the net exchange between land and atmosphere. Flooding forced a delay of ~3 weeks in crop planting, resulting in a notable shift in the seasonal cycle of photosynthetic uptake and a 15% lower peak rate. We estimate that the 2019 floods led to a reduction in Midwest cropland GPP of −0.21 PgC, which is partially compensated in August and September (+0.14 PgC). Top-down and bottom-up estimates of ΔCO_2 suggest a reduction of NEE of 0.1 PgC over June–July. Accounting for the entire growing season, the net effect of the floods results in a ~4% reduction in the annual cropland GPP. Focusing on the areas with cropland fractions larger than 50%, we predict a ~15% decline in crop productivity in 2019 relative to 2018.

This study provides strong evidence that our current space monitoring system is able to observe and quantify large regional perturbations in the carbon balance of terrestrial ecosystems. Given the extensive spatial coverage of OCO-2 and TROPOMI, these methods can be applied to monitor carbon cycle perturbation in remote locations where aircraft and ground-based inventories are not available. We envision that increased measurement frequency from future space-based observing systems, such as the GEOCarb mission (Moore et al., 2018), will allow for more accurate and precise near-real-time monitoring of extreme events affecting the terrestrial carbon cycle. We anticipate that such rapid, semiempirical event detection can benefit agricultural resource management (Atzberger, 2013; Weiss et al., 2020) and natural ecological forecasting efforts (Dietze et al., 2018). Detection of anomalies in GPP and NEE in near real time could be fed into a prognostic ecosystem model to improve prediction of regional agricultural or ecosystem anomalies. If such forecasting could be performed with sufficient skill, early planning could help mitigate the costs associated with variability in crop production. This would be analogous to the assimilation of atmospheric observations in a weather forecasting model.

Appendix A: Flux Inversion Setup

Flux inversions are performed with GHGF-Flux at 4° × 5° spatial resolution. Three flux inversions are performed that employ different prior NEE fluxes. For all inversions, we optimize 14-day scaling factors for daily net NEE and ocean fluxes, except for the final temporal grouping of the year, which is padded with 1 day. We use an assimilation window of approximately 18 months (October 7 to April 1 two years later). Initial conditions are generated from a previous flux inversion of OCO-2 measurements covering 2015–2017.

The optimized fluxes are taken to be the average of three flux inversions that employ different prior NEE fluxes and errors. Prior NEE fluxes are generated from three different models: SiB3 (Baker et al., 2008), CASA (Potter et al., 1993; James T Randerson et al., 1996; van der Werf et al., 2006), and FLUXCOM (Jung et al., 2017; Tramontana et al., 2016). SiB3 simulations used in this analysis use phenology (Leaf Area Index, LAI; fraction of Photosynthetically Active Radiation, fPAR) from the Moderate Resolution Imaging Spectroradiometer (MODIS). MERRA reanalysis is used as model inputs, with precipitation scaled to Global Precipitation Climatology Project (GPCP: Adler et al., 2003) following Baker et al. (2010). The version of CASA used here, CASA-GFED3, was modified from Potter et al. (1993) as described in Randerson et al. (1996) and van der Werf et al. (2006). It is driven by MERRA reanalysis and satellite observed NDVI to track plant phenology.

For all prior fluxes the annual total net flux has been adjusted to 4.6 PgC/year, to match the mean atmospheric CO2 growth rate. The diurnal cycle in NEE is prescribed using the modeled diurnal cycle from SiB3 for the SiB3 flux inversions and the diurnal cycle from CASA for the CASA and FLUXCOM inversions. The ECCO-Darwin-V1 model (Dutkiewicz et al., 2009; Menemenlis et al., 2008) estimates are used as the prior ocean CO_2 exchange for all inversions, and prior errors were taken to be 100% of the flux. Fossil fuel, biofuel, and biomass burning CO_2 emissions are prescribed using the Open-source Data Inventory for Anthropogenic CO_2, Version 2018 (Oda et al., 2018; Oda & Maksyutov, 2011) with downscaling to hourly emissions based on (Nassar et al., 2013), CASA-GFED4-FUEL, and Global Fire Emission Database, Version 4 (GFED4; Randerson et al., 2018) inventories, respectively.

Prior error covariance matrices are taken to be diagonal, such that there are no spatial or temporal covariances. The prior NEE errors are generated based on the NEE fluxes provided by the models. It is first taken to be 60% of the NEE flux. This is then increased by scaling up the errors at times and grid cells that have active vegetation but small net fluxes. For example, the uncertainty is scaled up during the spring (source to sink) and fall (sink to source) transition periods when the 14-day NEE flux is small, but the summer 14-day NEE fluxes are much larger. We also inflate the uncertainty for grid cells in which the flux is small for a given model but is much larger for the other models. The final errors range from 100% to 500% of the NEE flux.

We perform flux inversions that assimilate OCO-2 land nadir and land glint measurements. For assimilation, measurements are averaged into super-obs at $1° \times 1°$ spatial resolution following Liu et al. (2017), with the additional requirement that there must be a minimum of eight retrievals within each grid.

Data Availability Statement

TROPOMI and OCO-2 SIF products are accessed online (at https://data.caltech.edu/records/1347 (DOI: 10.22002/D1.1347) and https://oco2.gesdisc.eosdis.nasa.gov/data/OCO2_DATA/OCO2_L2_Lite_SIF.8r/). OCO-2 X_{CO2} retrieval files are downloaded from Jet Propulsion Laboratory (https://co2.jpl.nasa.gov/). ACT-America L2 in situ measurements can be downloaded from the ORNL DACC (https://doi.org/10.3334/ORNLDAAC/1556). County-level crop statistics is available at USDA NASS Quick Stats Database (https://quickstats.nass.usda.gov).

Acknowledgments
Part of this research was funded by the NASA Carbon Cycle Science program (Grants NNX17AE14G and NNH16ZDA001N) and the NASA OCO-2 Science Team (Grants 80NSSC18K0895 and NNH17ZDA001N). TROPOMI SIF data generation by P. K. and C. F. is funded by the Earth Science U.S. Participating Investigator program (Grant NNX15AH95G). Aircraft data is funded by the Atmospheric Carbon and Transport (ACT)-America Earth Venture Suborbital mission (grant NNX15AG76G to Penn State). B. B.'s research was supported by an appointment to the NASA Postdoctoral Program at the Jet Propulsion Laboratory, administered by Universities Space Research Association under contract with NASA. V.H. was supported by the Swiss National Science Foundation (P400P2_180784). Resources supporting this work were provided by the NASA High-End Computing (HEC) Program through the NASA Advanced Supercomputing (NAS) Division at Ames Research Center. Part of this research was carried out at the Jet Propulsion Laboratory, California Institute of Technology, under a contract with the National Aeronautics and Space Administration (80NM0018D0004).

References

Adler, R. F., Huffman, G. J., Chang, A., Ferraro, R., Xie, P. P., Janowiak, J., et al. (2003). The Version-2 global precipitation climatology Project714(GPCP) monthly precipitation analysis (1979–present). *Journal of Hydrometeorology*, *7154*(6), 1147–1167.

Atzberger, C. (2013, February). Advances in remote sensing of agriculture: Context description, existing operational monitoring systems and major information needs. *Remote Sensing*. https://doi.org/10.3390/rs5020949

Baker, I. T., Denning, A. S., & Stöckli, R. (2010). North American gross primary productivity: Regional characterization and interannual variability. *Tellus Series B: Chemical and Physical Meteorology*, *62*(5), 533–549. https://doi.org/10.1111/j.1600-0889.2010.00492.x

Baker, I. T., Prihodko, L., Denning, A. S., Goulden, M., Miller, S., & Da Rocha, H. R. (2008). Seasonal drought stress in the Amazon: Reconciling models and observations. *Journal of Geophysical Research – Biogeosciences*, *113*(G1).

Basu, S., Baker, D. F., Chevallier, F., Patra, P. K., Liu, J., & Miller, J. B. (2018). The impact of transport model differences on CO2 surface flux estimates from OCO-2 retrievals of column average CO 2. *Atmospheric Chemistry and Physics*, *18*(10).

Bolin, B. and Keeling, C. (1963). Large-scale atmospheric mixing as deduced from the seasonal and meridional variations of carbon dioxide. *Journal of Geophysical Research*, *68*(13):3899–3920, 0.1029/JZ068i013p03899.

Bowman, K. W., Liu, J., Bloom, A. A., Parazoo, N. C., Lee, M., Jiang, Z., et al. (2017). Global and Brazilian carbon response to El Niño Modoki 2011-2010. *Earth and Space Sci.*, *4*(10), 637–660. https://doi.org/10.1002/2016EA000204

Byrne, B., Jones, D. B. A., Strong, K., Polavarapu, S. M., Harper, A. B., Baker, D. F., & Maksyutov, S. (2019). On what scales can GOSAT flux inversions constrain anomalies in terrestrial ecosystems? *Atmospheric Chemistry and Physics*, *19*(20). https://doi.org/10.5194/acp-19-13017-2019

Byrne, B., Jones, D. B. A., Strong, K., Zeng, Z.-C., Deng, F., & Liu, J. (2017). Sensitivity of CO_2 surface flux constraints to observational coverage. *Journal of Geophysical Research*, *122*(12). https://doi.org/10.1002/2016JD026164

Byrne, B., Liu, J., Lee, M., Baker, I. T., Bowman, K. W., Deutscher, N. M., et al. (2019). Improved constraints on northern extratropical CO2 fluxes obtained by combining surface-based and space-based atmospheric CO2 measurements. *Earth and Space Science Open Archive.*. https://doi.org/10.1002/essoar.10501108.2

Byrne, B., Wunch, D., Jones, D. B. A., Strong, K., Deng, F., Baker, I., et al. (2018). Evaluating GPP and respiration estimates over northern midlatitude ecosystems using solar-induced fluorescence and atmospheric CO2 measurements. *Journal of Geophysical Research – Biogeosciences*, *123*(9), 2976–2997. https://doi.org/10.1029/2018JG004472

Ciais, P., Reichstein, M., Viovy, N., Granier, A., Ogée, J., Allard, V., et al. (2005). Europe-wide reduction in primary productivity caused by the heat and drought in 2003. *Nature*, *437*(7058), 529–533. https://doi.org/https://doi.org/10.1038/nature03972

Copernicus Climate Change Service (C3S) (2019). ERA5: Fifth generation of ECMWF atmospheric reanalyses of the global climate. *Copernicus Climate Change Service Climate Data Store (CDS)*.

Crisp, D., Fisher, B. M., O'Dell, C., Frankenberg, C., Basilio, R., Bösch, H., et al. (2012). The ACOS CO_2 retrieval algorithm—Part II: Global X_{CO2} data characterization. *Atmospheric Measurement Techniques*, *5*(4), 687–707. https://doi.org/10.5194/amt-5-687-2012

Dietze, M. C., Fox, A., Beck-Johnson, L. M., Betancourt, J. L., Hooten, M. B., Jarnevich, C. S., et al. (2018). Iterative near-term ecological forecasting: Needs, opportunities, and challenges. *Proceedings of the National Academy of Sciences of the United States of America*. https://doi.org/10.1073/pnas.1710231115

Digangi, J. P., Choi, Y., Nowak, J. B., Halliday, H. S., & Yang, M. M. (2017). *ACT-America: L2 In Situ Atmospheric CO_2, CO, CH_4, and O_3 Concentrations*. Eastern USA: ORNL DAAC. https://doi.org/10.3334/ORNLDAAC/1556

Dutkiewicz, S., Follows, M. J., & Bragg, J. G. (2009). Modeling the coupling of ocean ecology and biogeochemistry. *Global Biogeochem. Cy.*, *23*(4).

Feng, S., Lauvaux, T., Davis, K. J., Keller, K., Zhou, Y., Williams, C., et al. (2019). Seasonal characteristics of model uncertainties from biogenic fluxes, transport, and large-scale boundary inflow in atmospheric CO_2 simulations over North America. *Journal of Geophysical Research-Atmospheres*, 2019, *124*(24), 14,325–14,346. https://doi.org/10.1029/2019JD031165

Flechtner, F., Morton, P., Watkins, M., & Webb, F. (2014). Status of the GRACE follow-on mission. In *In Gravity, Geoid and Height Systems* (pp. 117–121). Cham Heidelberg New York Dordrecht London: Springer.

Frankenberg, C., & Berry, J. (2018). Solar induced chlorophyll fluorescence: Origins, relation to photosynthesis and retrieval. In *In Comprehensive Remote Sensing*, (pp. 143–162). Oxford: Elsevier. https://doi.org/10.1016/B978-0-12-409548-9.10632-3

Frankenberg, C., Fisher, J. B., Worden, J., Badgley, G., Saatchi, S. S., Lee, J.-E., et al. (2011). New global observations of the terrestrial carbon cycle from GOSAT: Patterns of plant fluorescence with gross primary productivity. *Geophysical Research Letters*, *38*(17), n/a–n/a. https://doi.org/10.1029/2011GL048738

Frankenberg, C., O'Dell, C., Guanter, L., & McDuffie, J. (2012). Remote sensing of near-infrared chlorophyll fluorescence from space in scattering atmospheres: Implications for its retrieval and interferences with atmospheric CO_2 retrievals. *Atmospheric Measurement Techniques*, *2*(8), 2081–2094. https://doi.org/10.5194/amt-5-2081-2012

Gelaro, R., McCarty, W., Suárez, M. J., Todling, R., Molod, A., Takacs, L., et al. (2017). The modern-era retrospective analysis for research and applications, version 2 (MERRA-2). *Journal of Climate*, *30*(14), 5419–5454. https://doi.org/10.1175/JCLI-D-16-0758.1

Green, J. K., Konings, A. G., Alemohammad, S. H., Berry, J., Entekhabi, D., Kolassa, J., et al. (2017). Regionally strong feedbacks between the atmosphere and terrestrial biosphere. *Nature Geoscience*, *10*(6), 410–414. https://doi.org/10.1038/ngeo2957

Green, J. K., Seneviratne, S. I., Berg, A. M., Findell, K. L., Hagemann, S., Lawrence, D. M., & Gentine, P. (2019). Large influence of soil moisture on long-term terrestrial carbon uptake. *Nature*, *565*(7740), 476–479. https://doi.org/10.1038/s41586-018-0848-x

Gu, L., Han, J., Wood, J. D., Chang, C., & Sun, Y. (2019). Sun-induced chlorophyll fluorescence and its importance for modeling photosynthesis from the side of light reactions. *The New Phytologist*. https://doi.org/10.1111/nph.15796

Guan, K., Berry, J. A., Zhang, Y., Joiner, J., Guanter, L., Badgley, G., & Lobell, D. B. (2016). Improving the monitoring of crop productivity using spaceborne solar-induced fluorescence. *Global Change Biology*, *22*(2), 716–726. https://doi.org/10.1111/gcb.13136

Guan, K., Pan, M., Li, H., Wolf, A., Wu, J., Medvigy, D., et al. (2015). Photosynthetic seasonality of global tropical forests constrained by hydroclimate. *Nature Geoscience*, *8*(4), 284–289. https://doi.org/10.1038/ngeo2382

Guanter, L., Zhang, Y., Jung, M., Joiner, J., Voigt, M., Berry, J. A., et al. (2014). Global and time-resolved monitoring of crop photosynthesis with chlorophyll fluorescence. *Proceedings of the National Academy of Sciences*, *111*(14), E1327–E1333. https://doi.org/10.1073/pnas.1320008111

Guerlet, S., Basu, S., Butz, A., Krol, M., Hahne, P., Houweling, S., et al. (2013). Reduced carbon uptake during the 2010 northern hemisphere summer from GOSAT. *Geophysical Research Letters*, *40*(10), 2378–2383. https://doi.org/10.1002/grl.50402

Gurney, K. R., Law, R. M., Denning, A. S., Rayner, P. J., Baker, D., Bousquet, P., et al. (2002). Towards robust regional estimates of CO_2 sources and sinks using atmospheric transport models. *Nature*, *415*(6872), 626–630. https://doi.org/10.1038/415626a

Hay, R. K. M. (1995). Harvest index: A review of its use in plant breeding and crop physiology. *The Annals of Applied Biology*, *126*(1), 197–216. https://doi.org/10.1111/j.1744-7348.1995.tb05015.x

He, L., Magney, T., Dutta, D., Yin, Y., Köhler, P., Grossmann, K., et al. (in review). From the ground to space: Using solar-induced fluorescence to estimate crop productivity. *Geophysical Research Letters*.

Hirabayashi, Y., Mahendran, R., Koirala, S., Konoshima, L., Yamazaki, D., Watanabe, S., et al. (2013). Global flood risk under climate change. *Nature Climate Change*, *3*(9), 816. Retrieved from–821. https://doi.org/10.1038/nclimate1911

Humphrey, V., Gudmundsson, L., & Seneviratne, S. I. (2016). Assessing global water storage variability from GRACE: Trends, seasonal cycle, subseasonal anomalies and extremes. *Surveys in Geophysics*, *37*(2), 357–395.

Humphrey, V., Zscheischler, J., Ciais, P., Gudmundsson, L., Sitch, S., & Seneviratne, S. I. (2018). Sensitivity of atmospheric CO_2 growth rate to observed changes in terrestrial water storage. *Nature*, *560*(7720), 628–631. https://doi.org/10.1038/s41586-018-0424-4

Ishizawa, M., Mabuchi, K., Shirai, T., Inoue, M., Morino, I., Uchino, O., et al. (2016). Inter-annual variability of summertime CO_2 exchange in northern Eurasia inferred from GOSAT X_{CO2}. *Environmental Research Letters*, *11*(10), 105001. https://doi.org/10.1088/1748-9326/11/10/105001

Jung, M., Reichstein, M., Schwalm, C. R., Huntingford, C., Sitch, S., Ahlström, A., et al. (2017). Compensatory water effects link yearly global land CO_2 sink changes to temperature. *Nature*, *541*(7638), 516–520. https://doi.org/10.1038/nature20780

Keenan, T. F., Migliavacca, M., Papale, D., Baldocchi, D., Reichstein, M., Torn, M., & Wutzler, T. (2019). Widespread inhibition of daytime ecosystem respiration. *Nature Ecology and Evolution.*, *3*(3), 407–415. https://doi.org/10.1038/s41559-019-0809-2

Keppel-Aleks, G., Wennberg, P. O., & Schneider, T. (2011). Sources of variations in total column carbon dioxide. *Atmospheric Chemistry and Physics*, *11*(8), 3581–3593. https://doi.org/10.5194/acp-11-3581-2011

Keppel-Aleks, G., Wennberg, P. O., Washenfelder, R. A., Wunch, D., Schneider, T., Toon, G. C., et al. (2012). The imprint of surface fluxes and transport on variations in total column carbon dioxide. *Biogeosciences*, *9*(3), 875–891. https://doi.org/10.5194/bg-9-875-2012

Köhler, P., Frankenberg, C., Magney, T. S., Guanter, L., Joiner, J., & Landgraf, J. (2018). Global retrievals of solar-induced chlorophyll fluorescence with TROPOMI: First results and intersensor comparison to OCO-2. *Geophysical Research Letters*, *45*(19), 10,410–456,463. https://doi.org/10.1029/2018GL079031

Landerer, F. W., & Swenson, S. C. (2012). Accuracy of scaled GRACE terrestrial water storage estimates. *Water Resources Research*, *48*(4), W04531. https://doi.org/10.1029/2011wr011453

Lauvaux, T., Schuh, A. E., Uliasz, M., Richardson, S., Miles, N., Andrews, A. E., et al. (2012). Constraining the CO_2 budget of the corn belt: Exploring uncertainties from the assumptions in a mesoscale inverse system. *Atmospheric Chemistry and Physics*, *12*(1), 337–354. https://doi.org/10.5194/acp-12-337-2012

Li, X., Xiao, J., He, B., Altaf Arain, M., Beringer, J., Desai, A. R., et al. (2018). Solar-induced chlorophyll fluorescence is strongly correlated with terrestrial photosynthesis for a wide variety of biomes: First global analysis based on OCO-2 and flux tower observations. *Global Change Biology*, *24*(9), 3990–4008. https://doi.org/10.1111/gcb.14297

Liu, J., Bowman, K., Parazoo, N. C., Bloom, A. A., Wunch, D., Jiang, Z., et al. (2018). Detecting drought impact on terrestrial biosphere carbon fluxes over contiguous US with satellite observations. *Environmental Research Letters*, *13*(9), 95003. https://doi.org/10.1088/1748-9326/aad5ef

Liu, J., Bowman, K. W., Lee, M., Henze, D. K., Bousserez, N., Brix, H., et al. (2014). Carbon monitoring system flux estimation and attribution: Impact of ACOS-GOSAT X_{CO2} sampling on the inference of terrestrial biospheric sources and sinks. *Tellus B*, *66*(1), 22486. https://doi.org/10.3402/tellusb.v66.22486

Liu, J., Bowman, K. W., Schimel, D. S., Parazoo, N. C., Jiang, Z., Lee, M., et al. (2017). Contrasting carbon cycle responses of the tropical continents to the 2015–2016 El Niño. *Science (New York, N.Y.)*, *358*(6360), eaam5690. https://doi.org/10.1126/science.aam5690

Liu, L., Guan, L., & Liu, X. (2017). Directly estimating diurnal changes in GPP for C3 and C4 crops using far-red Sun-induced chlorophyll fluorescence. *Agricultural and Forest Meteorology*, *232*, 1–9. https://doi.org/10.1016/j.agrformet.2016.06.014

MacBean, N., Maignan, F., Bacour, C., Lewis, P., Peylin, P., Guanter, L., et al. (2018). Strong constraint on modelled global carbon uptake using solar-induced chlorophyll fluorescence data. *Scientific Reports*, *8*(1), 1973. https://doi.org/10.1038/s41598-018-20024-w

Magney, T. S., Bowling, D. R., Logan, B. A., Grossmann, K., Stutz, J., Blanken, P. D., et al. (2019). Mechanistic evidence for tracking the seasonality of photosynthesis with solar-induced fluorescence. *Proceedings of the National Academy of Sciences of the United States of America*. https://doi.org/10.1073/pnas.1900278116,%20201900278

Magney, T. S., Frankenberg, C., Köhler, P., North, G., Davis, T. S., Dold, C., et al. (2019). Disentangling changes in the spectral shape of chlorophyll fluorescence: Implications for remote sensing of photosynthesis. *Journal of Geophysical Research – Biogeosciences*, *124*(6), 1491–1507. https://doi.org/10.1029/2019JG005029

Menemenlis, D., Campin, J.-M., Heimbach, P., Hill, C., Lee, T., Nguyen, A., et al. (2008). ECCO2: High resolution global ocean and sea ice data synthesis. *Mercator Ocean Quarterly Newsletter*, *31*(October), 13–21.

Miao, G., Guan, K., Yang, X., Bernacchi, C. J., Berry, J. A., DeLucia, E. H., et al. (2018). Sun-induced chlorophyll fluorescence, photosynthesis, and light use efficiency of a soybean field from seasonally continuous measurements. *Journal of Geophysical Research – Biogeosciences*, *123*(2), 610–623. https://doi.org/10.1002/2017JG004180

Miles, N. L., Richardson, S. J., Davis, K. J., Lauvaux, T., Andrews, A. E., West, T. O., et al. (2012). Large amplitude spatial and temporal gradients in atmospheric boundary layer CO_2 mole fractions detected with a tower-based network in the U.S. upper Midwest. *Journal of Geophysical Research – Biogeosciences*, *117*(G1). https://doi.org/10.1029/2011JG001781

Miller, C. E., Crisp, D., DeCola, P. L., Olsen, S. C., Randerson, J. T., Michalak, A. M., et al. (2007). Precision requirements for space-based data. *Journal of Geophysical Research-Atmospheres*, *112*(D10). https://doi.org/10.1029/2006JD007659

Moore, B., Crowell, S. M. R., Rayner, P. J., Kumer, J., O'Dell, C. W., O'Brien, D., et al. (2018). The potential of the geostationary carbon cycle observatory (GeoCarb) to provide multi-scale constraints on the carbon cycle in the Americas. *Frontiers in Environmental Science*, *6*, 109. https://doi.org/10.3389/fenvs.2018.00109

Mueller, N. D., Butler, E. E., McKinnon, K. A., Rhines, A., Tingley, M., Holbrook, N. M., & Huybers, P. (2016). Cooling of US Midwest summer temperature extremes from cropland intensification. *Nature Climate Change*, *6*(3), 317–322. https://doi.org/10.1038/nclimate2825

Nassar, R., Hill, T. G., McLinden, C. A., Wunch, D., Jones, D. B. A., & Crisp, D. (2017). Quantifying CO_2 emissions from individual power plants from space. *Geophysical Research Letters*, *44*(19), 10,10–45,53. https://doi.org/10.1002/2017GL074702

Nassar, R., Napier-Linton, L., Gurney, K. R., Andres, R. J., Oda, T., Vogel, F. R., & Deng, F. (2013). Improving the temporal and spatial distribution of CO_2 emissions from global fossil fuel emission data sets. *Journal of Geophysical Research-Atmospheres*, *118*(2), 917–933.

NOAA (October 2019). *National Centers for Environmental Information, Climate at a Glance: National Time Series, Published* Retrieve from https://www.ncdc.noaa.gov/cag/

Oda, T., & Maksyutov, S. (2011). A very high-resolution (1 km × 1 km) global fossil fuel CO2 emission inventory derived using a point source database and satellite observations of nighttime lights. *Atmospheric Chemistry and Physics*, *11*(2), 543–556.

Oda, T., Maksyutov, S., & Andres, R. J. (2018). The open-source data inventory for anthropogenic CO_2, version 2016 (ODIAC2016): A global monthly fossil fuel CO_2 gridded emissions data product for tracer transport simulations and surface flux inversions. *Earth System Science Data*, *10*(1), 87–107. https://doi.org/10.5194/essd-10-87-2018

Parazoo, N. C., Bowman, K., Fisher, J. B., Frankenberg, C., Jones, D. B. A., Cescatti, A., et al. (2014). Terrestrial gross primary production inferred from satellite fluorescence and vegetation models. *Global Change Biology*, *20*(10), 3103–3121. https://doi.org/10.1111/gcb.12652

Pérez-Priego, O., Guan, J.-H., Rossini, M., Fava, F., Wutzler, T., Moreno, G., et al. (2015). Sun-induced chlorophyll fluorescence and photochemical reflectance index improve remote-sensing gross primary production estimates under varying nutrient availability in a typical Mediterranean savanna ecosystem. *Biogeosciences*, *12*(21), 6351–6367. https://doi.org/10.5194/bg-12-6351-2015

Potter, C. S., Randerson, J. T., Field, C. B., Matson, P. A., Vitousek, P. M., Mooney, H. A., & Klooster, S. A. (1993). Terrestrial ecosystem production: A process model based on global satellite and surface data. *Global Biogeochem. Cy.*, *7*(4), 811–841. https://doi.org/10.1029/93GB02725

Randerson, J T, Van Der Werf, G. R., Giglio, L., Collatz, G. J., & Kasibhatla, P. S. (2018). Global Fire Emissions Database, Version 4.1 (GFEDv4). *ORNL DAAC*. https://doi.org/10.3334/ORNLDAAC/1293

Randerson, J. T., Thompson, M. V., Malmstrom, C. M., Field, C. B., & Fung, I. Y. (1996). Substrate limitations for heterotrophs: Implications for models that estimate the seasonal cycle of atmospheric CO_2. *Global Biogeochem. Cy.*, *10*(4), 585–602. https://doi.org/10.1029/96GB01981

Schuh, A. E., Jacobson, A. R., Basu, S., Weir, B., Baker, D., Bowman, K., et al. (2019). Quantifying the impact of atmospheric transport uncertainty on CO_2 surface flux estimates. *Global Biogeochem. Cy.*, *33*(4), 484–500.

Schuh, A. E., Lauvaux, T., West, T. O., Denning, A. S., Davis, K. J., Miles, N., et al. (2013). Evaluating atmospheric CO_2 inversions at multiple scales over a highly inventoried agricultural landscape. *Global Change Biology*, *19*(5), 1424–1439. https://doi.org/10.1111/gcb.12141

Schwandner, F. M., Gunson, M. R., Miller, C. E., Carn, S. A., Eldering, A., Krings, T., et al. (2017). Spaceborne detection of localized carbon dioxide sources. *Science*, *358*(6360), eaam5782.

Somkuti, P., Bösch, H., Feng, L., Palmer, P. I., Parker, R. J., & Quaife, T. (2020). A new space-borne perspective of crop productivity variations over the US Corn Belt. *Agricultural and Forest Meteorology*. https://doi.org/10.1016/j.agrformet.2019.107826

Sun, Y., Frankenberg, C., Jung, M., Joiner, J., Guanter, L., Köhler, P., & Magney, T. (2018). Overview of solar-induced chlorophyll fluorescence (SIF) from the orbiting carbon Observatory-2: Retrieval, cross-mission comparison, and global monitoring for GPP. *Remote Sensing of Environment*, *209*, 808–823. https://doi.org/10.1016/j.rse.2018.02.016

Sun, Y., Frankenberg, C., Wood, J. D., Schimel, D. S., Jung, M., Guanter, L., et al. (2017). OCO-2 advances photosynthesis observation from space via solar-induced chlorophyll fluorescence. *Science*, *358*(6360), eaam5747. https://doi.org/10.1126/science.aam5747

Sun, Y., Fu, R., Dickinson, R., Joiner, J., Frankenberg, C., Gu, L., et al. (2015). Drought onset mechanisms revealed by satellite solar-induced chlorophyll fluorescence: Insights from two contrasting extreme events. *Journal of Geophysical Research – Biogeosciences*, *120*(11), 2427–2440. https://doi.org/10.1002/2015JG003150

Tans, P. P., Crotwell, A. M., & Thoning, K. W. (2017). Abundances of isotopologues and calibration of CO_2 greenhouse gas measurements. *Atmospheric Measurement Techniques*, *10*(7), 2669–2685. https://doi.org/10.5194/amt-10-2669-2017

Tapley, B. D., Bettadpur, S., Ries, J. C., Thompson, P. F., & Watkins, M. M. (2004). GRACE measurements of mass variability in the earth system. *Science*, *305*(5683), 503–505. https://doi.org/10.1126/science.1099192

Thomison, P. R., Mullen, R. W., Lipps, P. E., Doerge, T., & Geyer, A. B. (2011). Corn response to harvest date as affected by plant population and hybrid. *Agronomy Journal*. https://doi.org/10.2134/agronj2011.0147

Tramontana, G., Jung, M., Schwalm, C. R., Ichii, K., Camps-Valls, G., Ráduly, B., et al. (2016). Predicting carbon dioxide and energy fluxes across global FLUXNET sites with regression algorithms. *Biogeosciences*, *13*(14), 4291–4313. https://doi.org/10.5194/bg-13-4291-2016

USDA United States Department of Agriculture (2019): Crop Progress, 22 Nov 2019, https://usda.library.cornell.edu/concern/publications/8336h188j?locale=en#release-items

van der Tol, C., Berry, J. A., Campbell, P. K. E., & Rascher, U. (2014). Models of fluorescence and photosynthesis for interpreting measurements of solar-induced chlorophyll fluorescence. *Journal of Geophysical Research – Biogeosciences*, *119*(12), 2312–2327. https://doi.org/10.1002/2014JG002713

van der Werf, G. R., Randerson, J. T., Giglio, L., Collatz, G. J., Kasibhatla, P. S., & Arellano, A. F. Jr. (2006). Interannual variability in global biomass burning emissions from 1997 to 2004. *Atmospheric Chemistry and Physics*, *6*(11), 3423–3441. https://doi.org/doi:10.5194/acp-6-3423-2006

Verma, M., Schimel, D., Evans, B., Frankenberg, C., Beringer, J., Drewry, D. T., et al. (2017). Effect of environmental conditions on the relationship between solar-induced fluorescence and gross primary productivity at an OzFlux grassland site. *Journal of Geophysical Research – Biogeosciences*, *122*(3), 716–733. https://doi.org/10.1002/2016JG003580

Wehr, R., Munger, J. W., McManus, J. B., Nelson, D. D., Zahniser, M. S., Davidson, E. A., et al. (2016). Seasonality of temperate forest photosynthesis and daytime respiration. *Nature*, *534*(7609), 680–683. https://doi.org/10.1038/nature17966

Weiss, M., Jacob, F., & Duveiller, G. (2020). Remote sensing for agricultural applications: A meta-review. *Remote Sensing of Environment*, *236*, 111402. https://doi.org/10.1016/j.rse.2019.111402

Wolf, S., Keenan, T. F., Fisher, J. B., Baldocchi, D. D., Desai, A. R., Richardson, A. D., et al. (2016). Warm spring reduced carbon cycle impact of the 2012 US summer drought. *Proceedings of the National Academy of Sciences*, *113*(21), 5880–5885. https://doi.org/10.1073/pnas.1519620113

Yang, X., Tang, J., Mustard, J. F., Lee, J.-E., Rossini, M., Joiner, J., et al. (2015). Solar-induced chlorophyll fluorescence that correlates with canopy photosynthesis on diurnal and seasonal scales in a temperate deciduous forest. *Geophysical Research Letters*, *42*(8), 2977–2987. https://doi.org/10.1002/2015GL063201

Yin, Y., Ciais, P., Chevallier, F., Li, W., Bastos, A., Piao, S., et al. (2018). Changes in the response of the northern hemisphere carbon uptake to temperature over the last three decades. *Geophysical Research Letters*, *45*(9), 4371–4380. https://doi.org/10.1029/2018GL077316

Yin, Y., Ciais, P., Chevallier, F., van der Werf, G. R., Fanin, T., Broquet, G., et al. (2016). Variability of fire carbon emissions in equatorial Asia and its non-linear sensitivity to El Niño. *Geophysical Research Letters*, *43*(19), 10,472–10,479. https://doi.org/10.1002/2016GL070971

Zhang, Y., Guanter, L., Berry, J. A., Joiner, J., van der Tol, C., Huete, A., et al. (2014). Estimation of vegetation photosynthetic capacity from space-based measurements of chlorophyll fluorescence for terrestrial biosphere models. *Global Change Biology*, *20*(12), 3727–3742. https://doi.org/10.1111/gcb.12664